Bioactive Materials 19 (2023) 12–23

Contents lists available at ScienceDirect

Bioactive Materials

journal homepage: www.keaipublishing.com/en/journals/bioactive-materials

Additively manufactured pure zinc porous scaffolds for critical-sized bone defects of rabbit femur

Dandan Xia [a,b], Yu Qin [c,d], Hui Guo [e], Peng Wen [c,d,**], Hong Lin [a,b,*], Maximilian Voshage [f], Johannes Henrich Schleifenbaum [f], Yan Cheng [g], Yufeng Zheng [e,***]

[a] Department of Dental Materials, Peking University School and Hospital of Stomatology, Beijing, 100081, China
[b] National Center of Stomatology, National Clinical Research Center for Oral Diseases, National Engineering Research Center of Oral Biomaterials and Digital Medical Devices, Beijing Key Laboratory of Digital Stomatology, Research Center of Engineering and Technology for Digital Dentistry Ministry of Health, NMPA Key Laboratory for Dental Materials, Beijing, 100081, China
[c] The State Key Laboratory of Tribology, Tsinghua University, Beijing, 100084, China
[d] Department of Mechanical Engineering, Tsinghua University, Beijing, 100084, China
[e] School of Materials Science and Engineering, Peking University, Beijing, 100871, China
[f] Digital Additive Production (DAP), RWTH Aachen University, 52074, Aachen, Germany
[g] Biomed-X Center, Academy for Advanced Interdisciplinary Studies, Peking University, Beijing, 100871, China

ARTICLE INFO

Keywords:
Additive manufacturing
Laser powder bed fusion
Scaffolds
Pure Zn
Critical-sized bone defect

ABSTRACT

Additive manufacturing has received attention for the fabrication of medical implants that have customized and complicated structures. Biodegradable Zn metals are revolutionary materials for orthopedic implants. In this study, pure Zn porous scaffolds with diamond structures were fabricated using customized laser powder bed fusion (L-PBF) technology. First, the mechanical properties, corrosion behavior, and biocompatibility of the pure Zn porous scaffolds were characterized *in vitro*. The scaffolds were then implanted into the rabbit femur critical-size bone defect model for 24 weeks. The results showed that the pure Zn porous scaffolds had compressive strength and rigidity comparable to those of cancellous bone, as well as relatively suitable degradation rates for bone regeneration. A benign host response was observed using hematoxylin and eosin (HE) staining of the heart, liver, spleen, lungs, and kidneys. Moreover, the pure Zn porous scaffold showed good biocompatibility and osteogenic promotion ability *in vivo*. This study showed that pure Zn porous scaffolds with customized structures fabricated using L-PBF represent a promising biodegradable solution for treating large bone defects.

1. Introduction

Critical-sized bone defects are a major challenge in orthopedics and are caused by trauma, tumor resection, or infection. Autografts are considered the gold standard for repairing large bone defects among clinically available grafts. However, autografts are rapidly absorbed prior to tissue repair. Moreover, problems caused by the limitations of donor sites and morbidity are often disturbing [1]. The effects of allografts, xenografts, and synthetic grafts are unsatisfactory owing to immune response complications, lack of osteogenic properties, and unfit anatomic shape and structure [2,3].

Additive manufacturing (AM) has revolutionized the traditional therapy of large bone defects by creating several different complex structures and shapes with high flexibility and efficiency [4,5]. Among different AM technologies, laser powder bed fusion (L-PBF) shows great potential for the manufacture of high-quality porous metal scaffolds [6] and is most widely used for fabricating fine structure porous metal bone implants [7]. AM has been successfully used to manufacture nondegradable porous scaffolds, such as stainless steel [8], Ti–6Al–4V [9] and tantalum [10]. These scaffolds have high compressive strength and excellent fatigue resistance. However, the need for secondary surgery and the potential to release harmful metal ions make these implants

Peer review under responsibility of KeAi Communications Co., Ltd.
* Corresponding author. Department of Dental Materials, Peking University School and Hospital of Stomatology, No.22, Zhongguancun South Avenue, Haidian District, Beijing, 100081, China.
** Corresponding author. The State Key Laboratory of Tribology, Tsinghua University, No.30 Shuangqing Road, HaiDian District, Beijing, 100084, China.
*** Corresponding author. School of Materials Science and Engineering, Peking University, No.5 Yi-He-Yuan Road, HaiDian District, Beijing, 100871, China.
E-mail addresses: wenpeng@tsinghua.edu.cn (P. Wen), hong196lin@bjmu.edu.cn (H. Lin), yfzheng@pku.edu.cn (Y. Zheng).

https://doi.org/10.1016/j.bioactmat.2022.03.010
Received 13 February 2022; Received in revised form 5 March 2022; Accepted 7 March 2022

inconvenient [11]. Moreover, nondegradable scaffolds take over mechanical and biological functions and cannot create additional space for new bone to grow into.

Biodegradable metals, including Mg-based, Zn-based, and Fe-based alloys, overcome the disadvantages of non-degradable metals [12,13]. Zn- and Zn-based alloys have better potential as porous scaffolds than Mg-based alloys owing to their unique degradation properties and mechanical strength. The standard electrode potential of Zn is between those of Mg and Fe; as a result, Zn is expected to exhibit an intermediate biodegradation rate. Moreover, the biodegradation products of Zn have good biocompatibility and do not generate hydrogen gas during degradation. Our recent study revealed that pure Zn membranes showed good osteogenic effects in rat skull critical-sized bone defects after week 10 [14]. Yang et al. [15] reported that bulk Zn, Zn-(Li, Mn, Mg, Ca, Sr, Fe, Ag) rods exhibited good biocompatibility after implantation into rat femora at week 8. Another recent study showed that bulk Zn–Sr alloys are biosafe and significantly promote bone regeneration in rat femoral chondral defects [16]. Biodegradable Zn is a new option for the fabrication of porous scaffolds to treat bone defects.

L-PBF is a new method for fabricating finely structured porous Zn scaffolds. However, the fabrication of Zn using L-PBF is challenging and potentially dangerous. Zn has a low melting point, high vapor pressure, and increased susceptibility to oxidation, all of which result in high material loss and poor fabrication conditions [17–19]. Severe evaporation of Zn during the L-PBF process can cause defects, including voids, splashing, sphere formation, lack of fusion, and rough surfaces [19]. For example, Zn parts that were intended to be completely dense formed porous structures with 12% porosity after the L-PBF process [20]. Researchers have investigated the effect of shielding gas flow on the surface quality and densification of bulk Zn during the L-PBF process [21], improving the forming quality of the pure Zn component. Recently, several research groups have successfully fabricated L-PBF porous Zn and their *in vitro* biodegradation, biocompatibility, and mechanical behavior were studied [22,23]. In our previous study, we fabricated Zn-xWE43 porous scaffolds and studied their formation quality, microstructure, and mechanical properties [24]. However, previous studies have mainly focused on *in vitro* properties, and the *in vivo* osteogenic performance and degradation behaviors of L-PBF pure Zn porous scaffolds are not known.

In this study, we hypothesized that pure Zn porous scaffolds with porous structures will have suitable strength while maintaining the biological advantages of porous structures. Consequently, we manufactured a pure Zn porous scaffold using the L-PBF technique and conducted a comprehensive study on the mechanical properties, degradation property, and *in vitro* biocompatibility of the L-PBF porous Zn scaffolds. We then implanted pure Zn porous scaffold into rabbit femur critical-sized bone defects and systematically evaluated its osteogenic capacity and degradation behavior *in vivo*.

2. Materials and methods

2.1. Design and AM of pure Zn porous scaffolds

Nitrogen-atomized pure Zn powder (Nanoval GmbH & Co. KG, Berlin, Germany) with an average particle size of 28.2 μm was prepared. Porous cylinders with diamond lattices were built with a strut size of 600 μm and pore size of 400 μm. These cylinders were the same as in a previous study to enable meaningful comparisons. The scaffolds were fabricated using a customized L-PBF machine (Aconity GmbH, Germany) with a single-mode ytterbium fiber laser (IPG YLR-400) and a maximum power of 400 W at a wavelength of 1070 μm. The key processing parameters, including the laser power (80 W), hatch spacing (70 μm), and powder layer thickness (30 μm), together determined the energy density (66.7 J/mm^3) used in this study. A gas circulation system was specially designed to eliminate the negative effects of evaporation, other harmful gases, and prevent oxidation [21,24]. Cylindrical samples of φ10 × 20 mm and φ6 × 9 mm were fabricated, for *in vitro* experiments and *in vivo* implantation, respectively. Finally, ultrasonic was used to remove the powder particles entrapped in the scaffolds, in absolute ethanol for 10 min. More details regarding the L-PBF equipment and procedures are provided in our previously published studies [17,21].

Pure bulk Zn ingots were fabricated by casting. The ingots were first homogenized by water quenching for 48 h at 320 °C. Then, they were hot extruded at 250 °C at an extrusion ratio of 25:1 and an extrusion speed of 1 mm/s.

2.2. Morphological characterization of pure Zn scaffolds

The top surface cross-section micromorphology of the L-PBF pure Zn scaffolds was observed using scanning electron microscopy (SEM, S-4800, Hitachi, Tokyo, Japan) combined with energy dispersive spectroscopy (EDS, X-Max 20, Oxford Instruments Inc., UK).

2.3. Mechanical tests

Compression tests were performed along the axis of the cylinder, on a universal material testing machine (Instron 5969, Norwood, USA) at a speed of 2 mm/min. Stress-strain curves were recorded. The yield strength is defined as the stress corresponding to 0.2% plastic deformation of the sample. The compressive yield strength (CYS) and ultimate compressive strength (UCS) were calculated based on the load–displacement curves. Five parallel samples were tested in each group.

2.4. Electrochemical experiments

A three-electrode electrochemical workstation (Autolab, Metrohm, Switzerland) was used, with the sample as the working electrode, a platinum electrode as the counter electrode, and a saturated calomel electrode as the reference electrode. The test process was conducted in Hanks' solution. Each sample underwent open circuit potential monitoring for 5400 s. Electrochemical impedance spectroscopy (EIS) measurements were performed by applying a 10 mV perturbation in the frequency range 10^5–10^{-2} Hz. Subsequently, potential dynamic polarization curves were measured at a scanning rate of 1 mV/s. The corrosion potential (E_{corr}) and corrosion current density (I_{corr}) were obtained from the polarization plots using Tafel analysis.

2.5. Immersion tests

To study the *in vitro* degradation performance of pure Zn scaffolds, immersion tests were performed in accordance with the ASTM-G31-72: Standard Practice for Laboratory Immersion Corrosion Testing of Metals. Briefly, the samples were immersed in Hank's solution at an immersion ratio of 20 mL/cm^2 at 37 °C for 60 days. The pH values were measured during immersion using a pH meter (S220–K, Mettler-Toledo Ltd., Switzerland). At the end of each period (3, 7, 14, 21, 28, and 60 days), the samples were washed with deionized water and dried in the open air. The surface morphologies and compositions of the corrosion products on the sample surfaces were analyzed using an SEM (JSM-IT100, JEOL Ltd, Japan) equipped with an EDS. To further identify the phases of the corrosion products, an X-ray diffractometer (XRD, Bruker D8 Advance diffractometer in Bragg-Brentano geometry) was used. The XRD was equipped with a graphite monochromator and a Vantec position-sensitive detector, and it was operated at 45 kV and 35 mA with a step size of 0.035° and a dwell time of 10 s/step using Co Kα radiation. The functional groups of the pure Zn scaffold were further detected using Fourier transform infrared spectroscopy (FTIR, Nicolet IS50, Thermo Fisher Scientific). The corrosion products were then removed using a chromic acid solution (200 g/L) with ultrasonic cleaning for 5 min. The degradation rate was calculated using the weight loss method: $C = (K \times \Delta W)/(A \times D \times T)$, where C is the degradation rate, mm/year; K

Table 1
Primer sequences in qPCR analysis.

Gene	Forward primer	Reverse primer
Runx2	5′-ACTACCAGCCACCGAGACCA-3′	3′-ACTGCTTGCAGCCTTAAATGACTCT-5′
ALP	5′- ATGGGATGGGTGTCTCCACA-3′	3′- CCACGAAGGGGAACTTGTC-5′
Osx	5′- ACTGCCCCACCCCTTAGACA-3′	3′- GAGGTGCACCCCCAAACCAA-5′
Ocn	5′-AGCCACCGAGACACCATGAGA-3′	3′- GGCTGCACCTTTGCTGGACT-5′
GAPDH	5′- AAGGTCGGAGTCAACGGATTTG-3′	3′- TCCTGGAAGATGGTGATGGGAT-5′

$= 8.76 \times 10^4$; ΔW is the mass loss, g; A is the surface area of the sample, cm^2; D is the sample density, g/cm^3; and T is the soaking time, hours). The ion concentrations (Zn^{2+}, Ca^{2+}, P^{5+}) in Hanks' solution were characterized by inductively coupled plasma-optical emission spectrometry (ICP-OES, iCAP 6300, Thermo, USA).

2.6. Cytocompatibility tests

Pure Zn scaffolds and bulk Zn extracts were prepared using α-minimal essential medium mixed with 10% fetal bovine serum for 24 h at an extraction ratio of 1 cm^2/mL in a cell incubator. The ion concentrations were measured using ICP-OES, and the pH values of the extracts were measured using a pH meter. The MC3T3-E1 cells were cultured in α-minimal essential medium mixed with 10% fetal bovine serum, 100 U/mL penicillin G, and 100 mg/mL streptomycin in a 100% relative humidity incubator (95% air, 5% CO_2, at 37 °C).

For the cell viability test, MC3T3-E1 cells (5×10^3) in 100 μL of the medium were seeded in 96-well plates. After 24 h, the medium was replaced with the alloy extracts (100%, 50%, and 10%) for 1, 3, and 5 days, respectively. The alloy extracts were then removed, and 10 μL CCK-8 solution (Dojindo Laboratories, Japan) was added to each well. The cells were then incubated for 1 h. The absorbance of each well was measured at 450 nm using a microplate reader (ELx800, Bio-Tek, VT, USA). The CCK-8 test was repeated three times, with five samples each.

To observe the effect of the pure Zn scaffold extracts on cell morphology, cells were seeded into 24-well plates and cultured for 24 h. Afterwards, they were gently washed with phosphate buffered saline (PBS) solution and fixed using 4% paraformaldehyde for 10 min at RT. Then, the cells were rinsed with PBS and permeabilized with 0.1% Triton X-100. Subsequently, the cells were stained with phalloidin-FITC (Sigma, USA) to label the cellular actin filaments and DAPI to label the cell nuclei. Specimens were observed and analyzed under a laser scanning confocal microscope (Zeiss Axiovert 650, Oberkochen, Germany) at excitation wavelengths of 488 and 405 nm.

2.7. Alkaline phosphatase (ALP) staining and quantification

To evaluate the effect of sample extracts on the early osteogenic differentiation marker ALP, human bone marrow mesenchymal stem-cells (hBMMSCs) were cultured in 12-well plates with sample extracts for 3 and 7 days. The cells were fixed in 4% paraformaldehyde and stained using the BCIP/NBT ALP Color Development Kit (Beyotime, China) for qualitative imaging. Pictures of each well were acquired using an optical microscope (BX51, Olympus, Japan). For the quantification of ALP activity, cells were rinsed with ice-cold PBS and then lysed in 1% Triton X-100 (Sigma, USA) for 10 min on ice. The cells were treated on ice with ultrasound and centrifuged at 12,000 g for 30 min at 4 °C. The protein concentration was measured by correlating the absorbance to protein concentration at 562 nm using a pre-plotted bovine albumin standard curve. The ALP activity was tested using the colorimetric production of p-nitrophenol via p-nitrophenyl phosphate/endogenous ALP enzymatic reaction (Jiancheng, Nanjing, China). Finally, ALP activity was normalized against the total intracellular protein content according to our previous study [25].

2.8. Real-time quantitative polymerase chain reaction (qPCR) analysis

The relative expression of osteogenic genes *ALP*, *Runx2*, *Ocn*, and *Osx* in hBMMSCs was analyzed by qPCR. Briefly, hBMMSCs were cultured in the extracts for 7 and 14 days. Total cellular RNA was extracted using TRIzol reagent (Invitrogen, USA), and RNA concentrations were determined using a spectrophotometer (NanoDrop 8000, Thermo, USA). RNA was reverse-transcribed into cDNA using a reverse transcription kit (TaKaRa, Japan). qPCR analysis was performed using the SYBR Green PCR Master Mix (Roche Applied Science, Germany) on a QuantStudio 3 Real-Time PCR detection system (Applied Biosystems, USA). Primers (Table 1) were designed according to cDNA sequences from the National Center for Biotechnology Information database. The relative mRNA expression levels of *ALP*, *Runx2*, and *Ocn* were normalized to those of the housekeeping gene glyceraldehyde 3-phosphate dehydrogenase. Cycle threshold values were used to calculate the fold change using the ΔΔCt method [26].

2.9. In vivo implantation

This experiment was approved by the Ethics Committee of the Peking University Health Science Center, Beijing, China (LA2019019). The procedures were conducted conforming to the protocol established by the Experimental Animal Ethics branch. To minimize suffering, fifteen New Zealand rabbits (5-months old, 2.5–3.0 kg, male) were anesthetized with pentobarbital sodium (30 mg/kg) via the ear vein and then locally injected with lidocaine into the femur. Bilateral critical-sized defects (6 mm in diameter and 9 mm in depth) were created in the femoral condyle using a dental drill, and normal saline was applied to cool the tissue. Pure Zn scaffolds were implanted into the predrilled defects. Finally, the incision was sutured using a non-absorbable thread. The rabbits were kept in an environmentally controlled house after the surgery.

Rabbit ear arterial blood was collected at weeks 4, 12, and 24 post-operatively. The rabbits were then sacrificed by an overdose of pentobarbital sodium, and the femora and organs (hearts, livers, spleens, lungs, and kidneys) were harvested. The concentrations of Zn^{2+} in the serum and fresh organs were measured using ICP-OES. The femora and the remaining organs were fixed in 10% buffered formalin for 24 h at RT. To evaluate alloy degradation and the healing status of the bone defect, X-ray and micro-computed tomography (micro-CT, 80 kVp, 500 μA, 1500 ms, Siemens, Germany) scans were performed. Multimodal visualization software (Inveon Research Workplace, Siemens, Germany) was used to perform the analyses.

After completing the micro-CT scan, hard tissue sections were made from the femora samples. Briefly, the femora were subjected to gradient dehydration and polymerization in polymethylmethacrylate resin. The samples were sliced to 200 μm using an EXAKT 300CP saw microtome and the sections were ground to 30–40 μm. Two sections were prepared for each sample. One section was sputter-deposited with a thin gold film and observed under an SEM (Hitachi S-4800, Japan) equipped with an EDS (Bruker QUANTAX, Germany) to investigate the changes in the structure and composition of the degradation layer. The other section was stained with methylene blue/acid fuchsin to observe the bone-implant contact area of the pure Zn porous scaffold.

The remaining femora samples were decalcified using 10% EDTA solution. Then, hematoxylin and eosin (HE) and Masson's trichrome

staining were performed. The organ samples were stained with HE. Finally, the stained sections were observed under an optical microscope (BX53, Olympus, Japan).

2.10. Statistical analysis

Statistical analysis was performed using the SPSS software (version 18.0; IBM, Armonk, NY, USA). The differences between each group were analyzed using an independent sample *t*-test and one-way analysis of variance (ANOVA). Statistical differences were considered significant if the *P*-value < 0.05.

3. Results

3.1. Morphological characterization and mechanical properties

Fig. 1(a) shows the longitudinal and cross 2D Micro-CT reconstruction images of the pure Zn porous scaffold, respectively. Fig. 1(c) shows the strut surfaces and cross-section, respectively, of the SEM images of the pure Zn porous scaffolds. Fig. 1(b) shows the compressive properties of the experimental pure Zn scaffold and bulk Zn. The compression curve (inset) shows a stable compression plateau after yielding. No sudden failures occurred. The CYSs of the pure zinc scaffold and bulk zinc were 14.9 ± 1.8 MPa and 25.1 ± 1.6 MPa, respectively, while the UCSs were 49.2 ± 2.1 MPa and 169.9 ± 2.5 MPa, respectively. The porous structure reduced the strength of the pure Zn scaffold compared with that of bulk Zn. The hardness values of the two types of pure Zn were similar.

3.2. In vitro degradation behavior

We characterized the transient degradation behaviors of the pure Zn scaffold and bulk Zn through electrochemical testing. As shown in Fig. 2(a), the polarization curves of both samples display a current plateau in the anode curve, indicating the passivation behavior of the samples during the degradation process. The corrosion potential (E_{corr}), corrosion current density (I_{corr}) and corrosion rate of the pure Zn scaffold were -1.29 ± 0.01 V, 71.39 ± 0.91 μA/cm^2 and 1.09 ± 0.02 mm/year, respectively. Compared to bulk Zn, the corrosion potential of the pure Zn scaffold decreased slightly, and its corrosion current density and corrosion rate accelerated. Moreover, the EIS responses of both specimens show that the semicircle radius of the pure Zn scaffold was less than that of bulk Zn, thus implying a decrease in corrosion resistance. These results highlight the reactivity of the pure Zn scaffold in Hank's solution over the initial few hours.

The degradation behavior was also tested using immersion tests. In the initial stage of immersion, the pure Zn scaffold degraded rapidly with increasing pH value and released Zn ion concentration in Hanks' solution, as shown in Fig. 3(a)–3(e). After 10 days, the pH of the solution remained unchanged. During the entire immersion process, the Zn ion concentration released by the pure Zn scaffold was higher than that released by bulk Zn, as shown in Fig. 3(b). Nevertheless, the ion concentrations of Ca and P in Hanks' solution were similar between the pure Zn scaffold and bulk Zn, with a slight reduction as shown in Fig. 3(c). After immersion for 60 days, Fig. 3(d) shows that the weight loss ratio of the pure Zn scaffold was $11.68 \pm 0.13\%$, and Fig. 3(e) shows that its degradation rate was 0.132 ± 0.004 mm/year.

We chose moderately corroded sections to qualitatively represent the performance of pure Zn scaffolds at 3, 7, 14, 21, 28, and 60 days. Fig. 4(a) shows the macro-morphologies of the pure Zn scaffold immersed in Hanks' solution. White degradation products were deposited on the surface of the pure Zn scaffold and gradually filled the scaffold pores. The corrosion SEM morphologies of the pure Zn scaffold showed that the pure Zn scaffold maintained their surface integrity with heavy product aggregation over the 60 day immersion period, as shown in Fig. 4(b). In addition, as shown in Fig. 4(c), EDS analysis showed that the corrosion layer of the external struts contained Zn, O, P, Ca, and C. The contents of P and Ca, as well as the Ca/P ratio, increased with time, indicating a tendency to produce zinc phosphate tetrahydrate and calcium phosphate salts. From the XRD shown in Fig. 4(d) and FTIR shown in Fig. 4(e), the degradation products mainly contained ZnO, a calcium phosphate salt of zinc, and $CaCO_3$.

3.3. Cytocompatibility

The cytocompatibility of the samples was tested by culturing MC3T3-E1 cells with pure Zn porous scaffolds and dense pure Zn extracts. The

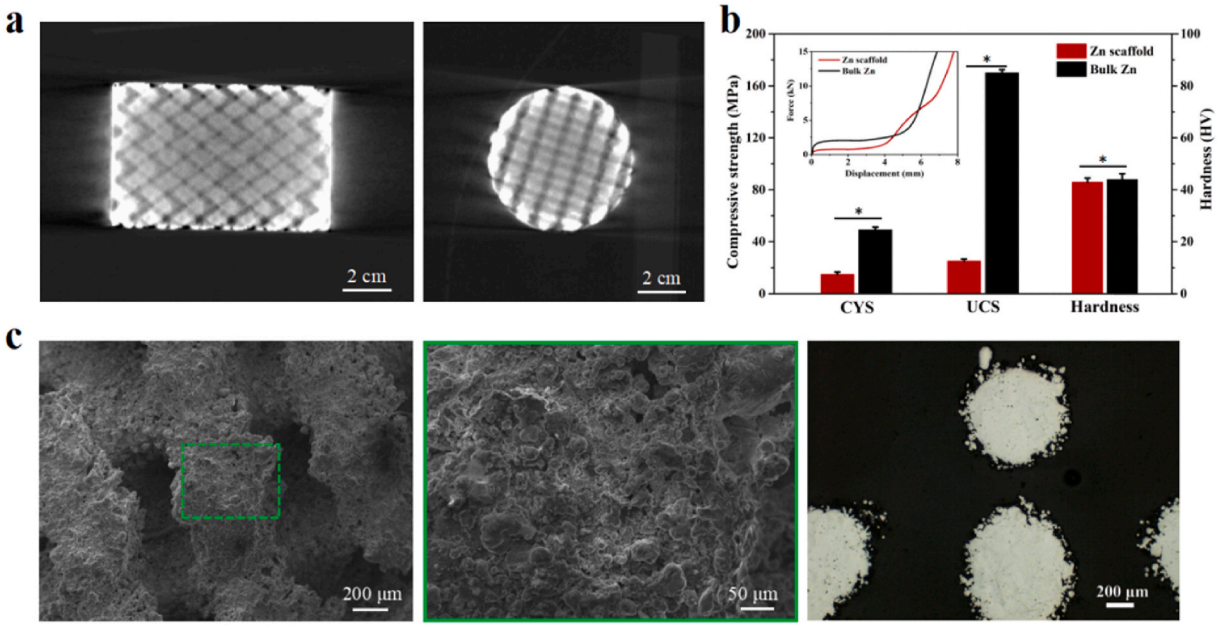

Fig. 1. (a) 2D Micro-CT reconstruction images of pure Zn porous scaffold; (b)Mechanical properties of pure Zn porous scaffold and dense pure Zn, CYS: compressive yield strength, UCS: ultimate compressive strength; (c) SEM images of pure Zn porous scaffold surface and cross-section. The data (n = 5) are expressed as mean ± standard deviation (SD). *: $P < 0.05$.

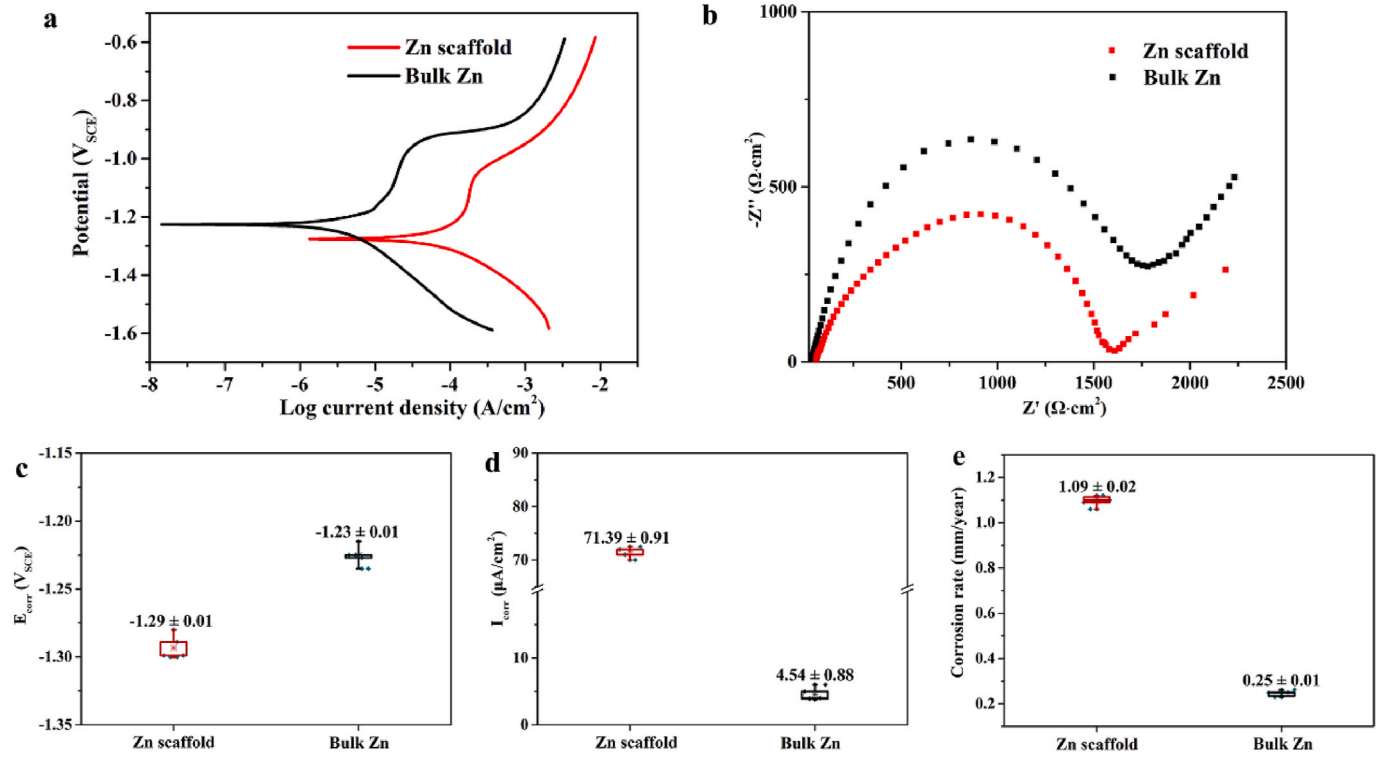

Fig. 2. Electrochemical test of pure Zn porous scaffold and dense pure Zn in Hanks' solution: (a) Potentiodynamic polarization curve; (b) Nyquist plot; (c) Corrosion potential (E_{corr}); (d) Corrosion current density (I_{corr}); (e) Corrosion rate.

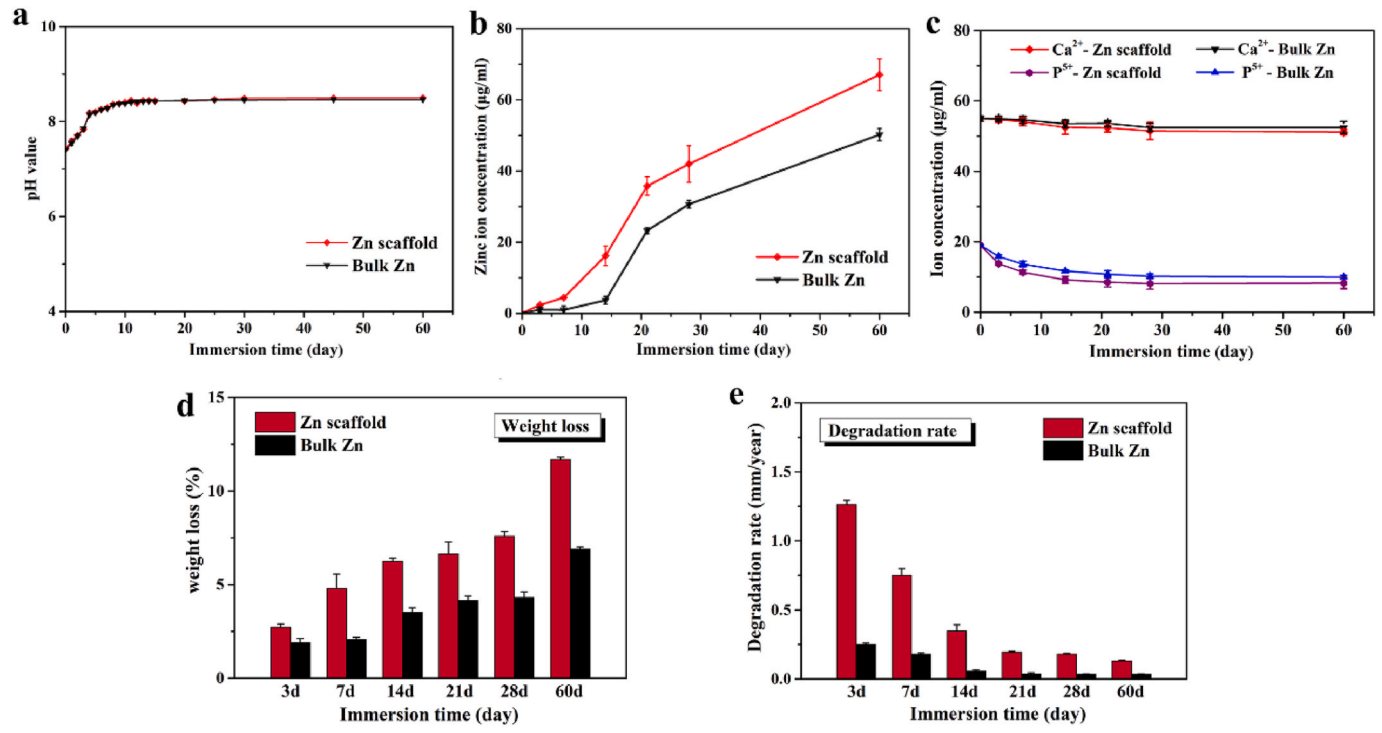

Fig. 3. *In vitro* degradation behavior of pure Zn porous scaffold and dense pure Zn immersed in Hank's solution during immersion for 60 days: (a) Evolution of pH values; (b) Zn ion concentration; (c) Ca and P ion concentration; (d) Weight loss ratio; (e) Degradation rate. The data (n = 5) are expressed as mean ± standard deviation (SD). *: $P < 0.05$.

relative activity of the cells in the extracts was compared with that of the blank control cell culture medium. As shown in Fig. 5(a), the viability of cells cultured in 100% extract medium was below 75% after 24 h, indicating a cytotoxic effect. As the culture time increased to 3 and 5 days, cell viability improved to above 75%. When extracts were diluted from 100% to 50% and 10%, the relative cell viability exceeded 75%,

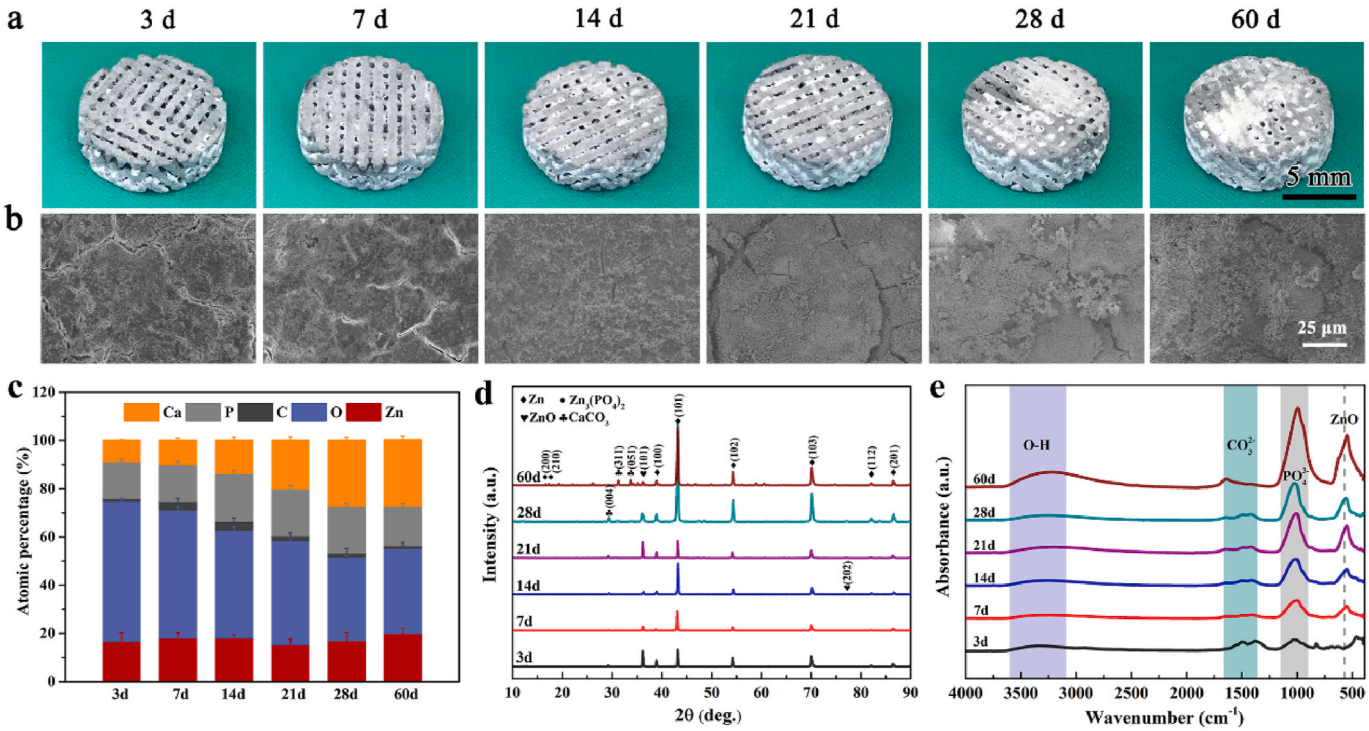

Fig. 4. Analysis of corrosion products of pure Zn porous scaffolds after being immersed in Hank's solution for 60 days: (a) Macro-morphologies; (b) Representative SEM images; (c) EDS analysis; (d) XRD; and (e) FTIR spectra of degradation products at different immersion time points.

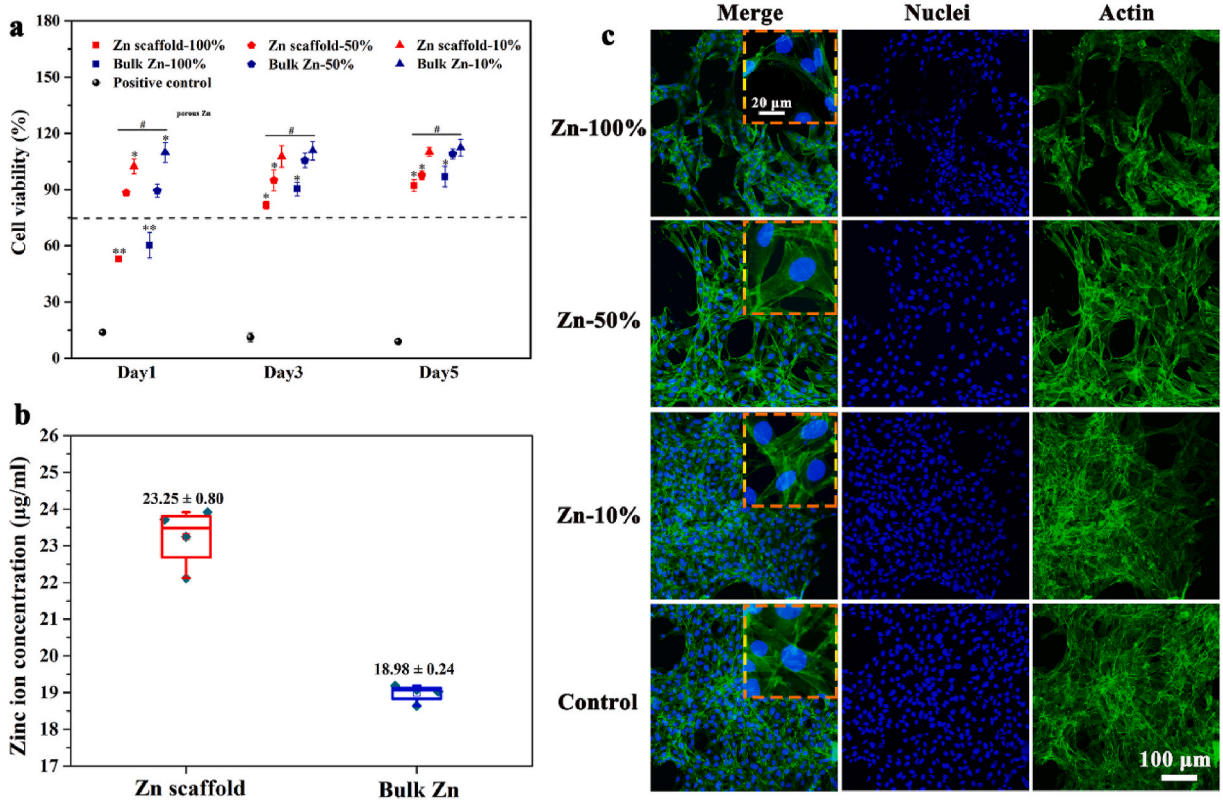

Fig. 5. Cytocompatibility of pure Zn porous scaffold and dense pure Zn extracts: (a) *In vitro* cytotoxicity test of MC3T3-E1 cells cultured in pure Zn porous scaffolds with and without dilution; (b) Zn ion concentrations after immersion in culture medium for 24 h; (c) Laser scanning confocal microscopy images of MC3T3-E1 cells cultured in pure Zn porous scaffold extracts with and without dilution. The actin cytoskeleton were stained green and the nuclei were stained blue. The data (n = 3) are expressed as mean ± standard deviation (SD). *: $P < 0.05$.

indicating that the cytocompatibility of the cells was significantly improved and became acceptable for biomedical use. The pure Zn porous scaffold showed a lower relative proliferation rate than dense pure Zn. The concentration of Zn ions in the pure Zn scaffold extract group was approximately 1.2 times than that of the pure bulk Zn group, as shown in Fig. 5(b).

The cell morphology at different extract concentrations was observed using a laser scanning confocal microscope. As shown in Fig. 5 (c), cells density in the 100% concentration extract were lower than the blank control group, which may be attributed to high Zn ion concentrations. Cells in the 50% and 10% extracts showed good spreading morphologies and clear cytoplasmic filaments. Moreover, the antennae between the cells were connected to each other, in a similar manner to that of the blank cell culture medium group. This trend is consistent with the cell viability results.

3.4. Osteogenic ability

The results of ALP staining in Fig. 6(a) and ALP activity in Fig. 6(b) showed that the 10% pure Zn scaffold extracts promoted the osteogenic differentiation of BMMSCs on days 3 and 7. The qPCR results in Fig. 6(c) showed that the 10% extract enhanced the expression of *ALP*, *Ocn*, *Osx*, and *Runx2* on days 7 and 14. Overall, the pure Zn scaffold promoted the osteogenic differentiation of BMMSCs *in vitro*.

3.5. In vivo results

The pure Zn porous scaffold in rabbit femur were visualized using micro-CT, histological analysis and SEM after weeks 4, 12, and 24. Fig. 7 (a) shows longitudinal section and cross-section of the scaffold 2D reconstruction images from micro-CT. Pure Zn scaffolds exhibited relatively intact shapes and no obvious degradation during the implantation time. The BV/TV and bone mineral density were measured, as shown in Fig. 7(b) and (c), respectively. With the extension of implantation time, the bone density around the implant increased, indicating that the growth of the bone tissue gradually matured. The volume change of the scaffold was calculated, as shown in Fig. 7(d). During implantation, the residual volume of the pure Zn scaffold gradually decreased. At week 24, the residual volume of the pure Zn scaffold was approximately 91 ± 0.68%. The results of methylene blue/basic fuchsin staining of the sections are shown in Fig. 7(e). After week 4 of implantation, a little new bone tissue was observed around the pure Zn scaffold, but there was a fibrous tissue layer between the bone tissue and the Zn scaffold. Twelve weeks after surgery, the newly formed bone matrix was in close contact with the scaffold. Moreover, new bone grew into the pores of the pure Zn porous scaffold. After week 24 of implantation, more new grew into the pores of the scaffolds, closely connected to the pure Zn porous scaffolds In addition, the pure Zn scaffold degraded gradually over time, giving rise to increased degradation products and decreased scaffold size.

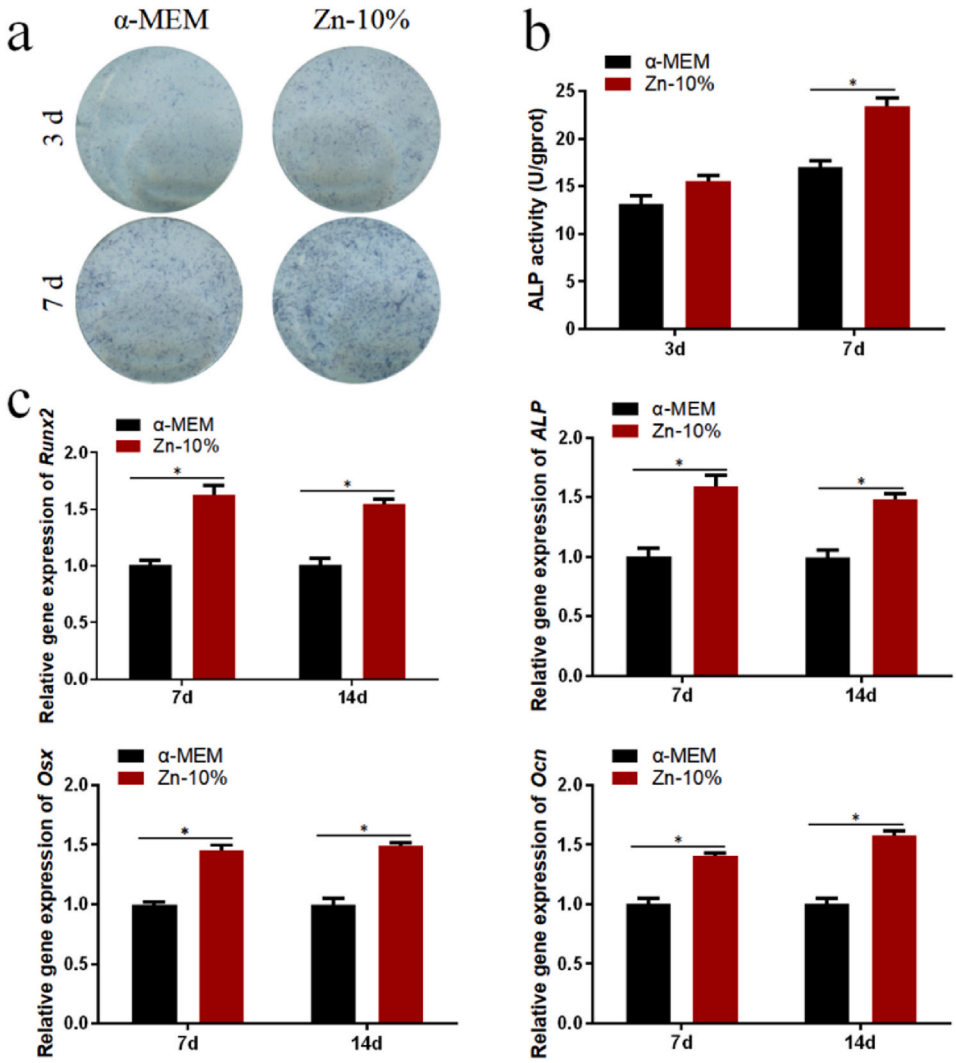

Fig. 6. Osteogenic capability of Zn porous scaffold extracts: (a) Alkaline phosphatase (ALP) staining at days 3 and 7; (b) ALP activity at days 3 and 7; (c) Eexpression of osteogenic genes (*Runx2, Ocn*, and *Osx*) of hBMMSCs at days 7 and 14. The data (n = 3) are expressed as mean ± standard deviation (SD). *: $P < 0.05$.

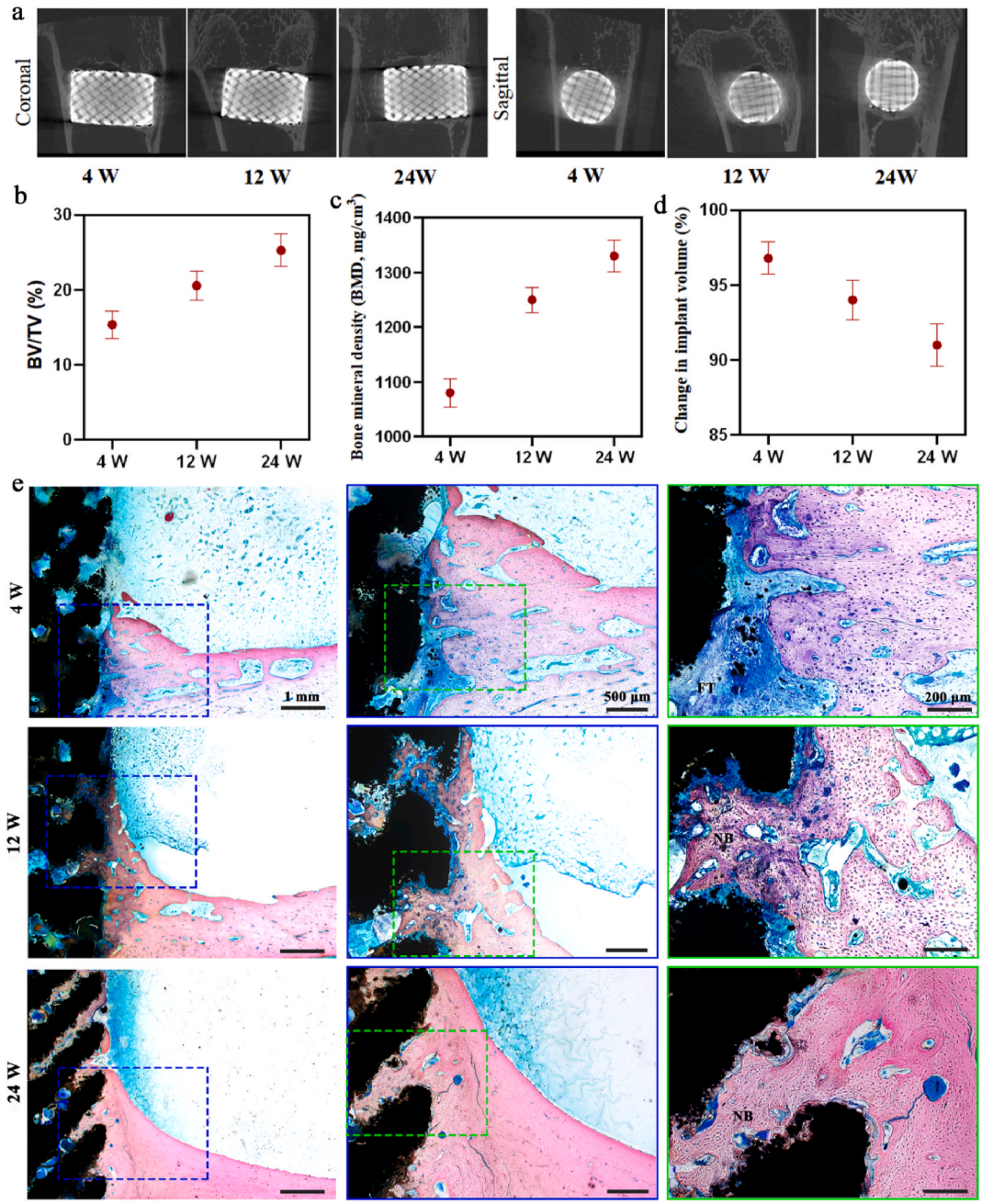

Fig. 7. *In vivo* rabbit femur bone defect evaluation after implantation for 4, 12, and 24 weeks. (a) Representative micro-CT images; (b) Quantitative volume fraction calculating new bone formation (BV/TV); (c) Bone mineral density; (d) Change of implant volume; (e) Hard tissue sections of methylene blue/basic fuchsin staining. NB, new bone; FT, fibrous tissue.

The decalcified sections of HE and Masson staining are shown in Fig. 8(a) and (b), respectively. Fibrous tissue could be seen clearly at week 4. At week 24, the fibrous tissue layer between the bone tissue and the Zn scaffold almost disappeared. No inflammatory reactions were observed during the observation period.

Fig. 9 displays the SEM and EDS images of the pure Zn porous scaffolds after weeks 4 and 12 of implantation. The pure Zn porous scaffold exhibited a uniform degradation pattern. At week 4, the scaffold surface was covered with a small amount of new bone. There was a gap between the scaffold and the bone tissue. The pure Zn scaffolds were covered by a degradation product layer, which was mainly composed of Zn, O, Ca, and P. At week 12, the pure Zn scaffolds were surrounded by thicker and denser newly formed bone. Besides, the degradation products of the pure Zn scaffolds were in close contact with the bone.

Optical images of HE stained sections of the organs are shown in the supplementary data. Fig. S1(a) shows that after week 24 of implantation, no significant pathological changes were observed in the heart, liver, spleen, lungs, and kidneys, indicating the biosafety of pure Zn scaffolds for the vital organs of rabbits. The Zn^{2+} concentration in the serum, heart, liver, spleen, lungs, and kidneys was maintained at normal levels and Fig. S1(b) shows that it was not significantly higher than that in the blank group during the observation period. This demonstrated that the pure Zn scaffold did not induce a significantly high concentration of serum Zn^{2+} or organ accumulation after implantation.

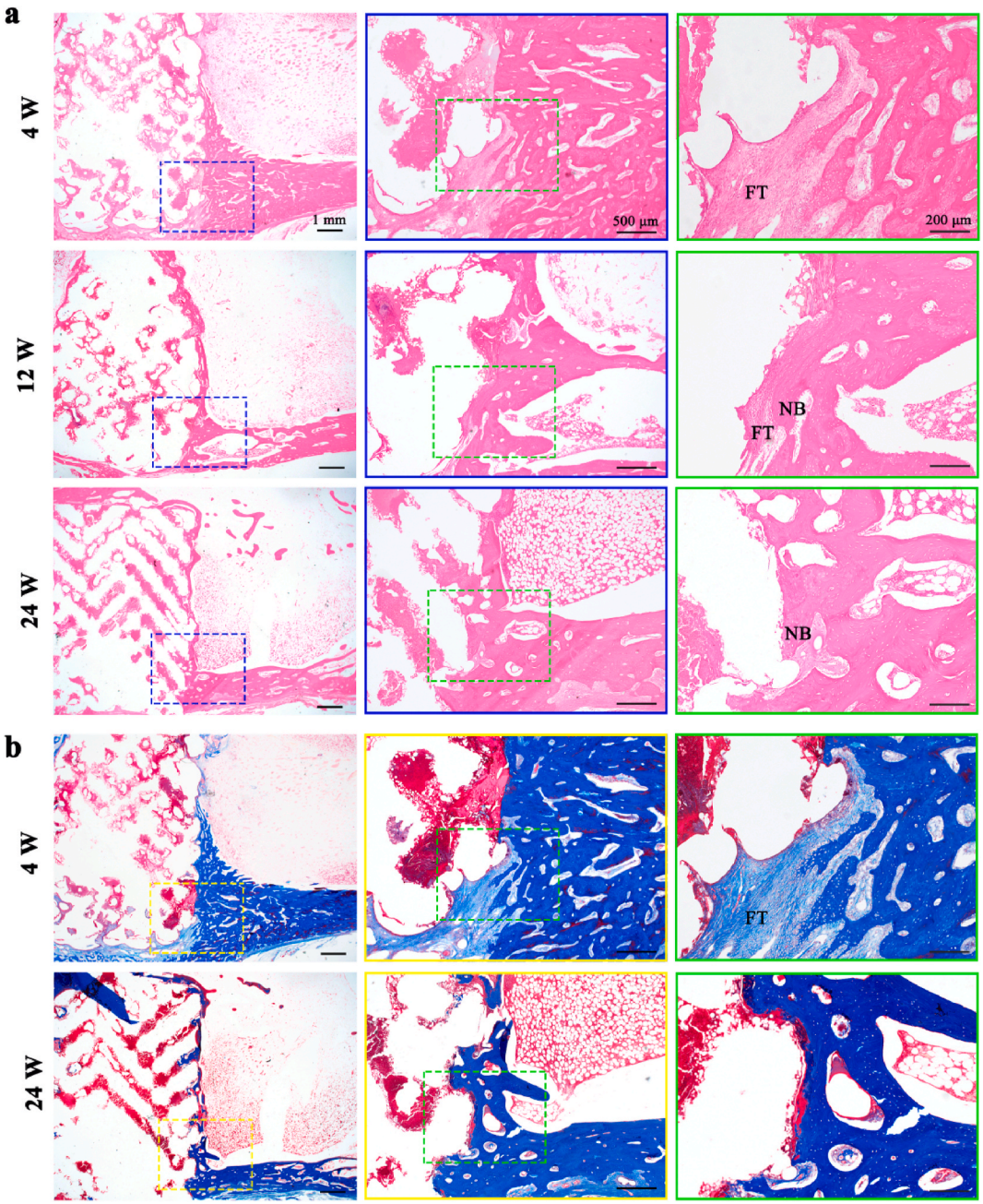

Fig. 8. Decalcified sections of femur after weeks 4, 12, and 24. (a) HE staining; (b) Masson's trichrome staining. NB, new bone; FT, fibrous tissue.

4. Discussion

An ideal bone scaffold should be biocompatible, biodegradable, and have mechanical strength similar to that of bone tissue [27]. The L-PBF pure Zn scaffolds in this study exhibited a well-designed structure, appropriate mechanical strength, and suitable biodegradation behavior for bone regeneration. Moreover, pure Zn scaffolds had good biocompatibility and promoted bone regeneration in rabbit critical-sized femur bone defect models.

4.1. Mechanical property

The mechanical properties of most bulk metallic implants are generally better than those of natural bones, leading to a stress shielding effect during long-term implantation. In this study, the pure Zn porous scaffold fabricated by L-PBF technology exhibited obviously reduced CYS (14.9 MPa) compared with bulk Zn prepared by the traditional manufacturing method (49.2 MPa). The elastic modulus of pure Zn scaffolds in our study was within that of human trabecular bones (0.01–2.0 GPa) [28], which provides appropriate mechanical support for bones and avoids the stress shielding effect. For L-PBF-produced Zn porous scaffolds, superior mechanical properties were achieved compared to modified casting methods [29]. The difference in the mechanical properties may be due to densification and grain size after L-PBF processing. The average grain size of pure Zn processed with L-PBF was 5.9 μm [30], while for the as-cast process, casting flaws often caused porosity, and the grain size was approximately 100 μm to more than 1000 μm [31]. Grain refinement significantly improves the mechanical properties of materials [32].

A well-designed scaffold structure is critical for recruiting cells from the surrounding bone and promoting nutrient diffusion and vascularization, which facilitates tissue regeneration [28]. Increased porosity and

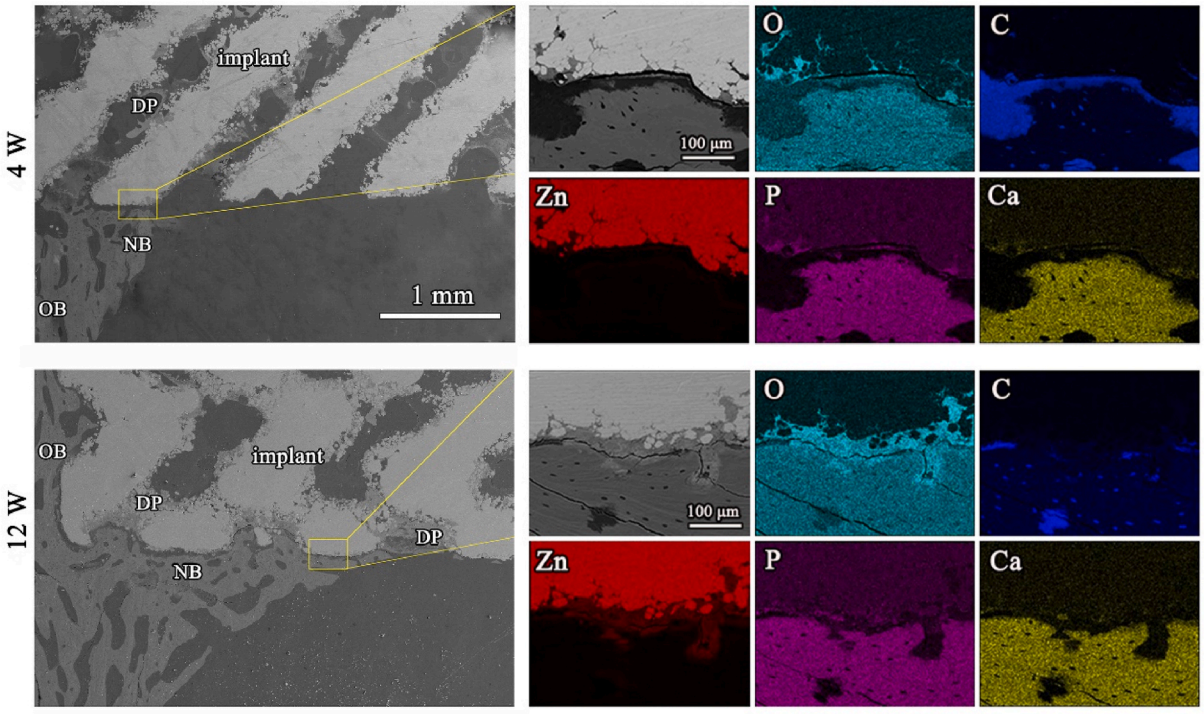

Fig. 9. SEM images coupled EDS mapping and analysis of the hard tissue cross sections after 4 and 12 weeks, with magnified images (yellow rectangles) and with corresponding elemental distribution visible: Zinc (green), Carbon (red), Oxygen (blue), Phosphate (yellow), Calcium (yellow), NB (new bone), OB (old bone), and DP (degradation products).

pore size promote bone ingrowth; however, this leads to reduced mechanical properties that compromise the structural integrity of the scaffolds [28], especially in load-bearing sites. Therefore, the upper limits of the scaffold structure are set by constraints related to the mechanical properties. Bai et al. reported that the maximum pore size for vascularization was 400 μm, beyond which no significant difference was observed [33]. However, Naoya et al. reported that bone growth of 600 μm porous Ti scaffolds in rabbit tibia tended to be higher than that of the 300 μm and 900 μm groups [34]. Similarly, Cove et al. reported that porous PLA scaffolds with 600 μm pore size exhibited higher cell proliferation and adhesion than 300 and 900 μm pore size [35]. Thus, in our study, we designed the pore size of pure Zn scaffolds to be 600 μm to achieve a balance between mechanical strength and biological function. Moreover, to achieve better performance, the mechanical properties of pure Zn scaffolds can be adjusted by structural design and further alloying treatment.

4.2. Degradation behavior

Complete bone regeneration usually takes 3–12 weeks for the upper limbs, and 12–24 weeks for the lower limbs [12]. Under ideal conditions, the degradation rate of scaffolds must match the bone formation rate, during which the scaffolds provide steady mechanical strength for 3–6 months and fully degrade in 1–2 years. This usually demands the degradation rate of bone implants to be approximately 0.2 mm/year [36,37]. The corrosion rate of the pure Zn scaffolds fabricated in our study was 0.132 ± 0.004 mm/year. Similarly, the corrosion rates of L-PBF Zn–Al parts were 0.13–0.16 mm/year [38]. Pure Zn scaffolds have a suitable corrosion rate for bone implants. In this study, no obvious corrosion pits or holes were detected on the surface as shown in Fig. 5 (a), indicating the relatively slight and uniform corrosion behavior of the pure Zn scaffold. The EDS analysis revealed that the degradation products of the pure Zn scaffold external struts contained Zn, O, P, Ca, and C elements as shown in Fig. 5(b). The contents of P and Ca, as well as the Ca/P ratio, increased with time, indicating a tendency to produce zinc phosphate tetrahydrate and calcium phosphate salts. Combined with the ICP results shown in Fig. 4(e), the Ca and P elements in the corrosion layer originate from Hanks' solution. This result is consistent with other studies that detected $Zn(OH)_2$, $Zn(PO4)_2{\cdot}4H_2O$, and $CaZn_2(PO_4)_2{\cdot}2H_2O$ in the Zn corrosion products [39]. A previous study reported the formation of ZnO, calcium/phosphorous phase, and zinc carbonate after implantation of pure Zn wire in the abdominal aorta of rats [40]. In another study, zinc oxide was the main component of degradation products [41].

4.3. Biocompatibility and osteogenic ability

The *in vitro* cell viability results showed that 100% pure Zn scaffold extracts were toxic to MC3T3-E1 cells, whereas diluted extracts showed improved and acceptable cytocompatibility. The 50% pure Zn scaffold extracts (178.8 μM) showed a stimulating effect on MC3T3-E1 cell proliferation, and the 10% pure Zn scaffold extracts (35.8 μM) exhibited a better proliferation promotion effect. The concentrations of Zn ions in undiluted extracts exceeded the tolerance limit of cells, causing toxicity effects in the cells. In the diluted extract group, cell viability was better than 80%, indicating acceptable cytocompatibility. A previous study reported that 50 μM zinc sulfate exhibited the best stimulatory effect on MC3T3-E1 cell proliferation, whereas Zn concentrations from 50 to 130 μM gradually diminished the stimulatory effect and led to cytotoxicity when the Zn^{2+} concentration was above 130 μM [39]. In another study, a Zn^{2+} concentration of 103.3 μM extracted from Zn-doped calcium phosphate cement improved mBMMSC proliferation [40]. The diverse results may be due to the difference in the sensitivity of the cell type, cell culture medium, or a different volume of extraction medium. Previous research has recommended a minimal 6–10 times dilution of magnesium extracts for *in vitro* cytotoxicity tests [41]. Therefore, the *in vitro* biocompatibility of the pure Zn scaffold was guaranteed.

In vivo implantation of pure Zn scaffold showed good biocompatibility, unlike the toxic effect of the 100% extracts *in vitro*. This trend is consistent with previous studies showing that the *in vivo*

biocompatibility results are better than that of the *in vitro* results [14,42]. The reason for this phenomenon may be that the degradation products of pure Zn scaffolds are rapidly diluted by body fluid compared to *in vitro* static culture conditions. The *in vivo* degradation process of pure Zn scaffolds is relatively complex owing to a more complex environment containing a variety of ions, proteins, and cells. In a previous study, pure Zn wires implanted into the abdominal aorta of male Sprague-Dawley rats showed good biocompatibility and ideal physiological corrosion behavior during long-term implantation [43]. Another study found that pure Zn and binary Zn-(Li, Mn, Mg, Ca, Sr, Fe, Ag) rods exhibited good biocompatibility in rat femora [12]. In yet another study, a Zn–Li–Sr alloy showed acceptable biocompatibility both *in vitro* and *in vivo* [44]. As previously reported, Zn has the least toxicity in bone metabolism compared with other trace elements [45].

At week 4, there was a fibrous tissue layer between the scaffold and bone tissue. At week 12, the newly formed bone grew into the pores of the scaffold, and the fibrous connective tissue layer became thinner. At week 24, the newly formed bone was well integrated into the Zn porous scaffolds. Immediately after implantation, the host response began, including overlapping stages of tissue injury, inflammation, proliferation, and tissue remodeling [46,47]. Implants alter the progress and outcome of each stage [46]. Successful implantation largely depends on the host response, especially inflammatory responses at the host-implant interface. Once the biomaterial is implanted into the body, the implant is instantly covered by an adsorbed layer, typically plasma protein [48], which causes rapid degradation of pure Zn scaffolds and the burst release of degradation products. The tissue response is closely related to the degradation products of pure Zn scaffolds, including Zn ions, hydroxide ions, oxides, and Ca/P compounds. Appropriate concentrations of degradation products can have beneficial effects on the host response, whereas high concentrations of corrosion products may disturb the local physiological equilibrium at the implantation site, resulting in adverse effects on the surrounding tissue [49]. In the early stages of implantation, the relatively high concentrations of degradation products exceeded the tolerance of the body. This can explain the fibrous tissue formation between the bone tissue and scaffolds at week 4. Similar results were reported for fibrotic tissue between bone tissue and pure Zn or Zn/HA composites, indicating a lack of direct osseointegration after week 8 of implantation [50]. As the bone healing process proceeded, the degradation rate of the pure Zn scaffold slowed owing to reduced inflammation and less fluid. At weeks 12 and 24, the newly formed bone matrix was in closer contact with the scaffold and even grew into the pores of the scaffolds. Thus, the current *in vivo* study provides evidence that pure Zn scaffolds exhibit osteogenic ability for bone regeneration.

The bone formation phenomenon ability may be attributed to the dual function of osteoconduction and osteoinduction of the pure Zn scaffolds. On the one hand, the pure Zn scaffolds serve as guiding cues to direct bone growth, owing to the ability of osteoconduction for three-dimensional scaffolds [51]; On the other hand, the osteoinduction property of pure Zn degradation products, especially Zn^{2+}. Previous studies reported that Zn^{2+} can induce ectopic bone formation in canine muscle in a dose-dependent manner [52]. Another study showed that zinc enhances ATPase activity and regulates the transcription of osteoblast differentiation-related genes such as ALP, osteopontin, osteocalcin, and type I collagen [53]. Moreover, Zn is crucial for promoting bone formation by activating protein synthesis in osteoblasts [54]. The extracellular Zn^{2+} promotes osteogenesis by entering the BMSCs through endocytosis and activating the ERK pathway [55]. The detailed osteogenic mechanisms of pure Zn scaffolds require further exploration.

5. Conclusions

Pure Zn porous scaffolds were successfully fabricated using L-PBF for large bone defects. Further, the *in vitro* and *in vivo* performances of the pure Zn scaffolds were systematically studied. The L-PBF pure Zn scaffolds showed relatively suitable degradation rates (0.132 ± 0.004 mm/year) and mechanical strength (CYS, 14.9 MPa; UCS, 22.9 MPa; elastic modulus, 0.95 GPa) for bone implants. Moreover, pure Zn scaffolds exhibited good *in vitro* cytocompatibility with MC3T3-E1 cells and osteogenic ability for hBMMSCs. The *in vivo* implantation results showed that the pure Zn scaffolds have the potential for large bone defect applications with osteogenic properties. Therefore, L-PBF pure Zn porous scaffolds are promising candidates for bone regeneration.

CRediT authorship contribution statement

Dandan Xia: Investigation, Data curation, Writing – original draft. **Yu Qin:** Investigation, Data curation. **Hui Guo:** Investigation, Data curation. **Peng Wen:** Writing – review & editing, Resources, Supervision, Funding acquisition. **Hong Lin:** Resources, Supervision, Funding acquisition. **Maximilian Voshage:** Writing – review & editing. **Johannes Henrich Schleifenbaum:** Writing – review & editing. **Yan Cheng:** Writing – review & editing. **Yufeng Zheng:** Conceptualization, Writing – review & editing, Resources, Supervision, Funding acquisition, Project administration.

Declaration of competing interest

The authors declared that they have no conflicts of interest to this paper. We declare that we do not have any commercial or associative interest that represents a conflict of interest in connection with this paper.

Acknowledgments

This work was supported by the National Key R&D Program of China [grant number 2018YFE0104200]; the National Natural Science Foundation of China [grant numbers 51901003, 51931001, 52171233, 51875310]; the Beijing Natural Science Foundation [grant number L212014]; and the Open Project of NMPA Key Laboratory for Dental Materials [grant number PKUSS20200401].

Appendix A. Supplementary data

Supplementary data to this article can be found online at https://doi.org/10.1016/j.bioactmat.2022.03.010.

References

[1] J.F. Keating, A. Simpson, C.M. Robinson, The management of fractures with bone loss, J. Bone Joint Surg.-Br. 87B (2) (2005) 142–150, https://doi.org/10.1302/0301-620x.87b2.15874.
[2] R. Dimitriou, E. Jones, D. McGonagle, P.V. Giannoudis, Bone regeneration: current concepts and future directions, BMC Med. 9 (2011), https://doi.org/10.1186/1741-7015-9-66.
[3] W. Wang, K.W.K. Yeung, Bone grafts and biomaterials substitutes for bone defect repair: a review, Bioactive materials 2 (4) (2017) 224–247, https://doi.org/10.1016/j.bioactmat.2017.05.007.
[4] N. Jones, Science in three dimensions: the print revolution, Nature 487 (7405) (2012) 22–23, https://doi.org/10.1038/487022a.
[5] B. Derby, Printing and prototyping of tissues and scaffolds, Science 338 (6109) (2012) 921–926, https://doi.org/10.1126/science.1226340.
[6] L. Yuan, S. Ding, C. Wen, Additive manufacturing technology for porous metal implant applications and triple minimal surface structures: a review, Bioactive materials 4 (1) (2019) 56–70, https://doi.org/10.1016/j.bioactmat.2018.12.003.
[7] S.L. Sing, J. An, W.Y. Yeong, F.E. Wiria, Laser and electron-beam powder-bed additive manufacturing of metallic implants: a review on processes, materials and designs, J. Orthop. Res.: official publication of the Orthopaedic Research Society 34 (3) (2016) 369–385, https://doi.org/10.1002/jor.23075.
[8] Y.M. Wang, T. Voisin, J.T. McKeown, J. Ye, N.P. Calta, Z. Li, Z. Zeng, Y. Zhang, W. Chen, T.T. Roehling, R.T. Ott, M.K. Santala, P.J. Depond, M.J. Matthews, A. V. Hamza, T. Zhu, Additively manufactured hierarchical stainless steels with high strength and ductility, Nat. Mater. 17 (1) (2018) 63–71, https://doi.org/10.1038/nmat5021.
[9] D.A. Hollander, M. von Walter, T. Wirtz, R. Sellei, B. Schmidt-Rohlfing, O. Paar, H.-J. Erli, Structural, mechanical and in vitro characterization of individually structured Ti-6Al-4V produced by direct laser forming, Biomaterials 27 (7) (2006) 955–963.

[10] R. Wauthle, J. van der Stok, S. Amin Yavari, J. Van Humbeeck, J.P. Kruth, A. A. Zadpoor, H. Weinans, M. Mulier, J. Schrooten, Additively manufactured porous tantalum implants, Acta Biomater. 14 (2015) 217–225, https://doi.org/10.1016/j.actbio.2014.12.003.

[11] S. Bose, M. Roy, A. Bandyopadhyay, Recent advances in bone tissue engineering scaffolds, Trends Biotechnol. 30 (10) (2012) 546–554, https://doi.org/10.1016/j.tibtech.2012.07.005.

[12] Y. Zheng, X. Gu, F. Witte, Biodegradable metals, Mater. Sci. Eng. R Rep. 77 (2014) 1–34, https://doi.org/10.1016/j.mser.2014.01.001.

[13] Y. Liu, Y. Zheng, X.H. Chen, J.A. Yang, H. Pan, D. Chen, L. Wang, J. Zhang, D. Zhu, S. Wu, K.W.K. Yeung, R.C. Zeng, Y. Han, S. Guan, Fundamental theory of biodegradable metals—definition, criteria, and design, Adv. Funct. Mater. 29 (18) (2019), https://doi.org/10.1002/adfm.201805402.

[14] H. Guo, D. Xia, Y. Zheng, Y. Zhu, Y. Liu, Y. Zhou, A pure zinc membrane with degradability and osteogenesis promotion for guided bone regeneration: in vitro and in vivo studies, Acta Biomater. 106 (2020) 396–409, https://doi.org/10.1016/j.actbio.2020.02.024.

[15] H. Yang, B. Jia, Z. Zhang, X. Qu, G. Li, W. Lin, D. Zhu, K. Dai, Y. Zheng, Alloying design of biodegradable zinc as promising bone implants for load-bearing applications, Nat. Commun. 11 (1) (2020) 401, https://doi.org/10.1038/s41467-019-14153-7.

[16] B. Jia, H. Yang, Z. Zhang, X. Qu, X. Jia, Q. Wu, Y. Han, Y. Zheng, K. Dai, Biodegradable Zn-Sr alloy for bone regeneration in rat femoral condyle defect model: in vitro and in vivo studies, Bioactive materials 6 (6) (2021) 1588–1604, https://doi.org/10.1016/j.bioactmat.2020.11.007.

[17] P. Wen, L. Jauer, M. Voshage, Y.Z. Chen, R. Poprawe, J.H. Schleifenbaum, Densification behavior of pure Zn metal parts produced by selective laser melting for manufacturing biodegradable implants, J. Mater. Process. Technol. 258 (2018) 128–137, https://doi.org/10.1016/j.jmatprotec.2018.03.007.

[18] P. Wen, M. Voshage, L. Jauer, Y.Z. Chen, Y. Qin, R. Poprawe, J.H. Schleifenbaum, Laser additive manufacturing of Zn metal parts for biodegradable applications: processing, formation quality and mechanical properties, Mater. Des. 155 (2018) 36–45, https://doi.org/10.1016/j.matdes.2018.05.057.

[19] Y. Qin, P. Wen, H. Guo, D. Xia, Y. Zheng, L. Jauer, R. Poprawe, M. Voshage, J. H. Schleifenbaum, Additive manufacturing of biodegradable metals: current research status and future perspectives, Acta Biomater. 98 (2019) 3–22, https://doi.org/10.1016/j.actbio.2019.04.046.

[20] M. Montani, A.G. Demir, E. Mostaed, M. Vedani, B. Previtali, Processability of pure Zn and pure Fe by SLM for biodegradable metallic implant manufacturing, Rapid Prototyp. J. 23 (3) (2017) 514–523, https://doi.org/10.1108/rpj-08-2015-0100.

[21] P. Wen, Y. Qin, Y.Z. Chen, M. Voshage, L. Jauer, R. Poprawe, J.H. Schleifenbaum, Laser additive manufacturing of Zn porous scaffolds: shielding gas flow, surface quality and densification, J. Mater. Sci. Technol. 35 (2) (2019) 368–376, https://doi.org/10.1016/j.jmst.2018.09.065.

[22] K. Lietaert, A.A. Zadpoor, M. Sonnaert, J. Schrooten, L. Weber, A. Mortensen, J. Vleugels, Mechanical properties and cytocompatibility of dense and porous Zn produced by laser powder bed fusion for biodegradable implant applications, Acta Biomater. 110 (2020) 289–302, https://doi.org/10.1016/j.actbio.2020.04.006.

[23] Y. Li, P. Pavanram, J. Zhou, K. Lietaert, P. Taheri, W. Li, H. San, M.A. Leeflang, J. M.C. Mol, H. Jahr, A.A. Zadpoor, Additively manufactured biodegradable porous zinc, Acta Biomater. 101 (2020) 609–623, https://doi.org/10.1016/j.actbio.2019.10.034.

[24] Y. Qin, P. Wen, M. Voshage, Y.Z. Chen, P.G. Schuckler, L. Jauer, D.D. Xia, H. Guo, Y.F. Zheng, J.H. Schleifenbaum, Additive manufacturing of biodegradable Zn-xWE43 porous scaffolds: formation quality, microstructure and mechanical properties, Mater. Des. 181 (2019), https://doi.org/10.1016/j.matdes.2019.107937. ARTN 107937.

[25] W. Ge, Y. Liu, T. Chen, X. Zhang, L. Lv, C. Jin, Y. Jiang, L. Shi, Y. Zhou, The epigenetic promotion of osteogenic differentiation of human adipose-derived stem cells by the genetic and chemical blockade of histone demethylase LSD1, Biomaterials 35 (23) (2014) 6015–6025, https://doi.org/10.1016/j.biomaterials.2014.04.055.

[26] W. Ge, L. Shi, Y. Zhou, Y. Liu, G.E. Ma, Y. Jiang, Y. Xu, X. Zhang, H. Feng, Inhibition of osteogenic differentiation of human adipose-derived stromal cells by retinoblastoma binding protein 2 repression of RUNX2-activated transcription, Stem Cell. 29 (7) (2011) 1112–1125, https://doi.org/10.1002/stem.663.

[27] G. Turnbull, J. Clarke, F. Picard, P. Riches, L. Jia, F. Han, B. Li, W. Shu, 3D bioactive composite scaffolds for bone tissue engineering, Bioactive materials 3 (3) (2018) 278–314, https://doi.org/10.1016/j.bioactmat.2017.10.001.

[28] V. Karageorgiou, D. Kaplan, Porosity of 3D biomaterial scaffolds and osteogenesis, Biomaterials 26 (27) (2005) 5474–5491, https://doi.org/10.1016/j.biomaterials.2005.02.002.

[29] I. Cockerill, Y. Su, S. Sinha, Y.-X. Qin, Y. Zheng, M.L. Young, D. Zhu, Porous zinc scaffolds for bone tissue engineering applications: a novel additive manufacturing and casting approach, Mater. Sci. Eng. Mater. Biol. Appl. 110 (2020) 110738, https://doi.org/10.1016/j.msec.2020.110738.

[30] Y. Qin, P. Wen, D. Xia, H. Guo, M. Voshaged, L. Jauerd, Y. Zheng, J. Henrich S, Effect of grain structure on the mechanical properties and in vitro corrosion behavior of additively manufactured pure Zn, Additive Manufacturing 33 (2020) 101134, https://doi.org/10.1016/j.addma.2020.101134.

[31] J. Kubasek, D. Vojtech, E. Jablonska, I. Pospisilova, J. Lipov, T. Ruml, Structure, mechanical characteristics and in vitro degradation, cytotoxicity, genotoxicity and mutagenicity of novel biodegradable Zn-Mg alloys, Mater. Sci. Eng. Mater. Biol. Appl. 58 (2016) 24–35, https://doi.org/10.1016/j.msec.2015.08.015.

[32] Z.L. Liu, A new approach toward designing and synthesizing the microalloying Zn biodegradable alloys with improved mechanical properties, Metall. Mater. Trans. 50A (1) (2019) 311–325, https://doi.org/10.1007/s11661-018-4978-4.

[33] F. Bai, Z. Wang, J. Lu, J. Liu, G. Chen, R. Lv, J. Wang, K. Lin, J. Zhang, X. Huang, The correlation between the internal structure and vascularization of controllable porous bioceramic materials in vivo: a quantitative study, Tissue Eng. 16 (12) (2010) 3791–3803, https://doi.org/10.1089/ten.tea.2010.0148.

[34] N. Taniguchi, S. Fujibayashi, M. Takemoto, K. Sasaki, B. Otsuki, T. Nakamura, T. Matsushita, T. Kokubo, S. Matsuda, Effect of pore size on bone ingrowth into porous titanium implants fabricated by additive manufacturing: an in vivo experiment, Materials science & engineering, Mater. Biol. Appl. 59 (2016) 690–701, https://doi.org/10.1016/j.msec.2015.10.069.

[35] M. Cavo, S. Scaglione, Scaffold microstructure effects on functional and mechanical performance: integration of theoretical and experimental approaches for bone tissue engineering applications, Mater. Sci. Eng. Mater. Biol. Appl. 68 (2016) 872–879, https://doi.org/10.1016/j.msec.2016.07.041.

[36] Y. Chen, Z. Xu, C. Smith, J. Sankar, Recent advances on the development of magnesium alloys for biodegradable implants, Acta Biomater. 10 (11) (2014) 4561–4573, https://doi.org/10.1016/j.actbio.2014.07.005.

[37] C. Shuai, S. Li, S. Peng, P. Feng, Y. Lai, C. Gao, Biodegradable metallic bone implants, Mater. Chem. Front. 3 (4) (2019) 544–562, https://doi.org/10.1039/c8qm00507a.

[38] C.J. Shuai, Y. Cheng, Y.W. Yang, S.P. Peng, W.J. Yang, F.W. Qi, Laser additive manufacturing of Zn-2Al part for bone repair: formability, microstructure and properties, J. Alloys Compd. 798 (2019) 606–615, https://doi.org/10.1016/j.jallcom.2019.05.278.

[39] D. Liang, M. Yang, B. Guo, J. Cao, L. Yang, X. Guo, Zinc upregulates the expression of osteoprotegerin in mouse osteoblasts MC3T3-E1 through PKC/MAPK pathways, Biol. Trace Elem. Res. 146 (3) (2012) 340–348, https://doi.org/10.1007/s12011-011-9254-z.

[40] K. Xiong, J. Zhang, Y.Y. Zhu, L. Chen, J.D. Ye, Zinc doping induced differences in the surface composition, surface morphology and osteogenesis performance of the calcium phosphate cement hydration products, Mater. Sci. Eng. Mater. Biol. Appl. 105 (2019), https://doi.org/10.1016/j.msec.2019.110065.

[41] J. Wang, F. Witte, T. Xi, Y. Zheng, K. Yang, Y. Yang, D. Zhao, J. Meng, Y. Li, W. Li, K. Chan, L. Qin, Recommendation for modifying current cytotoxicity testing standards for biodegradable magnesium-based materials, Acta Biomater. 21 (2015) 237–249, https://doi.org/10.1016/j.actbio.2015.04.011.

[42] Y. Su, H. Yang, J. Gao, Y.X. Qin, Y. Zheng, D. Zhu, Interfacial zinc phosphate is the key to controlling biocompatibility of metallic zinc implants, Adv. Sci. 6 (14) (2019) 1900112, https://doi.org/10.1002/advs.201900112.

[43] P.K. Bowen, J. Drelich, J. Goldman, Zinc exhibits ideal physiological corrosion behavior for bioabsorbable stents, Adv. Mater. 25 (18) (2013) 2577–2582, https://doi.org/10.1002/adma.201300226.

[44] Z. Zhang, B. Jia, H. Yang, Y. Han, Q. Wu, K. Dai, Y. Zheng, Zn0.8Li0.1Sr-a biodegradable metal with high mechanical strength comparable to pure Ti for the treatment of osteoporotic bone fractures: in vitro and in vivo studies, Biomaterials 275 (2021) 120905, https://doi.org/10.1016/j.biomaterials.2021.120905.

[45] M. Yamaguchi, Role of nutritional zinc in the prevention of osteoporosis, Mol. Cell. Biochem. 338 (1–2) (2010) 241–254, https://doi.org/10.1007/s11010-009-0358-0.

[46] J.M. Anderson, A. Rodriguez, D.T. Chang, Foreign body reaction to biomaterials, Semin. Immunol. 20 (2) (2008) 86–100, https://doi.org/10.1016/j.smim.2007.11.004.

[47] Y. Chandorkar, K. Ravikumar, B. Basu, The foreign body response demystified, ACS Biomater. Sci. Eng. 5 (1) (2019) 19–44, https://doi.org/10.1021/acsbiomaterials.8b00252.

[48] D.F. Williams, On the mechanisms of biocompatibility, Biomaterials 29 (20) (2008) 2941–2953, https://doi.org/10.1016/j.biomaterials.2008.04.023.

[49] D. Hong, P. Saha, D.T. Chou, B. Lee, B.E. Collins, Z. Tan, Z. Dong, P.N. Kumta, In vitro degradation and cytotoxicity response of Mg-4% Zn-0.5% Zr (ZK40) alloy as a potential biodegradable material, Acta Biomater. 9 (10) (2013) 8534–8547, https://doi.org/10.1016/j.actbio.2013.07.001.

[50] H. Yang, X. Qu, W. Lin, C. Wang, D. Zhu, K. Dai, Y. Zheng, In vitro and in vivo studies on zinc-hydroxyapatite composites as novel biodegradable metal matrix composite for orthopedic applications, Acta Biomater. 71 (2018) 200–214, https://doi.org/10.1016/j.actbio.2018.03.007.

[51] F.E. Weber, Reconsidering osteoconduction in the era of additive manufacturing, Tissue Eng. B Rev. 25 (5) (2019) 375–386, https://doi.org/10.1089/ten.teb.2019.0047.

[52] X.M. Luo, D. Barbieri, N. Davison, Y.G. Yan, J.D. de Bruijn, H.P. Yuan, Zinc in calcium phosphate mediates bone induction: in vitro and in vivo model, Acta Biomater. 10 (1) (2014) 477–485, https://doi.org/10.1016/j.actbio.2013.10.011.

[53] I.-S. Kwun, Y.-E. Cho, R.-A.R. Lomeda, H.-I. Shin, J.-Y. Choi, Y.-H. Kang, J. H. Beattie, Zinc deficiency suppresses matrix mineralization and retards osteogenesis transiently with catch-up possibly through Runx 2 modulation, Bone 46 (3) (2010) 732–741, https://doi.org/10.1016/j.bone.2009.11.003.

[54] M. Yamaguchi, Role of zinc in bone formation and bone resorption, J. Trace Elem. Exp. Med. 11 (2–3) (1998) 119–135, https://doi.org/10.11299/brte.18.346.

[55] X.M. Gao, Y.Y. Xue, Z. Zhu, J.Y. Chen, Y.H. Liu, X.T. Cheng, X. Zhang, J. Wang, X. B. Pei, Q.B. Wan, Nanoscale zeolitic imidazolate framework-8 activator of canonical MAPK signaling for bone repair, ACS Appl. Mater. Interfaces 13 (1) (2021) 97–111, https://doi.org/10.1021/acsami.0c15945.